MIT Libraries | DSpace@MIT

MIT Open Access Articles

Charged particle diagnostics for inertial confinement fusion and high-energy-density physics experiments

Massachusetts Institute of Technology

Charged particle diagnostics for inertial confinement fusion and high-energy-density physics experiments

🆔 **M. Gatu Johnson**

COLLECTIONS

Paper published as part of the special topic on Diagnostics for inertial confinement fusion

View Online   **Export Citation**   **CrossMark**

ARTICLES YOU MAY BE INTERESTED IN

Neutron imaging of inertial confinement fusion implosions
Review of Scientific Instruments **94**, 021101 (2023); https://doi.org/10.1063/5.0124074

Invited article: X-ray phase contrast imaging in inertial confinement fusion and high energy density research
Review of Scientific Instruments **94**, 021103 (2023); https://doi.org/10.1063/5.0127497

Soft x-ray power diagnostics for fusion experiments at NIF, Omega, and Z facilities
Review of Scientific Instruments **94**, 031101 (2023); https://doi.org/10.1063/5.0131949

Charged particle diagnostics for inertial confinement fusion and high-energy-density physics experiments

View Online   Export Citation   CrossMark

M. Gatu Johnson[a] (ID)

AFFILIATIONS

Massachusetts Institute of Technology, Cambridge, Massachusetts 02139, USA

Note: Paper published as part of the Special Topic on Diagnostics for inertial confinement fusion.
[a]Author to whom correspondence should be addressed: gatu@psfc.mit.edu

ABSTRACT

MeV-range ions generated in inertial confinement fusion (ICF) and high-energy-density physics experiments carry a wealth of information, including fusion reaction yield, rate, and spatial emission profile; implosion areal density; electron temperature and mix; and electric and magnetic fields. Here, the principles of how this information is obtained from data and the charged particle diagnostic suite currently available at the major US ICF facilities for making the measurements are reviewed. Time-integrating instruments using image plate, radiochromic film, and/or CR-39 detectors in different configurations for ion counting, spectroscopy, or emission profile measurements are described, along with time-resolving detectors using chemical vapor deposited diamonds coupled to oscilloscopes or scintillators coupled to streak cameras for measuring the timing of ion emission. A brief description of charged-particle radiography setups for probing subject plasma experiments is also given. The goal of the paper is to provide the reader with a broad overview of available capabilities, with reference to resources where more detailed information can be found.

I. INTRODUCTION

Charged particle (ion) diagnostics have been widely used for inertial confinement fusion (ICF) and high-energy-density physics (HEDP) experiments for decades. The MeV-range ions detected with these instruments are generated in fusion reactions, scattering reactions, or laser–plasma interactions, and carry key information about, e.g., ICF implosion fusion yield and reaction rate, spatial emission profile, or fuel and shell areal density (ρR). MeV-range ions are also frequently used as a backlighter to probe conditions in a subject plasma experiment. The charged particle diagnostic suite can additionally be used for basic nuclear physics experiments to study nuclear reactions using the ICF platform.

In the US, this currently includes experiments at the OMEGA,[1] OMEGA "extended performance" (EP),[2] and National Ignition Facility[3] (NIF), including with the Advanced Radiographic Capability (ARC), lasers. Charged particle diagnostic capabilities also exist at short pulse laser facilities under the LaserNetUS umbrella,[4] but this

is a separate topic, which will not be covered in the present review. Historically, a suite of charged particle diagnostics was developed and extensively used for the intense ion beam inertial confinement fusion program at Sandia National Laboratories (SNL).[5]

Previous reviews include a 2003 paper specifically focused on charged particle spectrometry (Séguin *et al.*, Ref. 6) and a 2020 review more broadly covering nuclear diagnostics for these facilities (Frenje, Ref. 7). The present paper covers charged particle diagnostics, including for counting (yield) applications, spectrometry, time-resolved bang time and burn history, emission profile, and imaging measurements. These measurements are closely related to, and often compared with, fusion yield measurements using neutron activation detectors (see, e.g., Ref. 8 and references therein), neutron spectrometry, reviewed in Ref. 9, and neutron imaging, reviewed in Ref. 10.

The paper is organized as follows: In Sec. II, relevant charged-particle-producing reactions and processes in ICF and HEDP plasmas are summarized, and information obtainable from the study

of the reaction products is discussed. Section III describes detector types commonly used for time-integrated charged-particle measurements, including image plates (IP), radiochromic film (RCF), and CR-39 solid-state nuclear track detectors. Section IV discusses spectrometry using energy information from CR-39 track sizes, Sec. V magnet-based spectrometers, and Sec. VI Thomson parabola instruments. In Sec. VII, spatial profile measurements are discussed, and time-resolved measurements are reviewed in Sec. VIII. Section IX gives a brief description of proton radiography platforms and the detectors used for such measurements. Section X concludes the discussion.
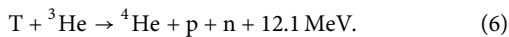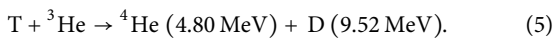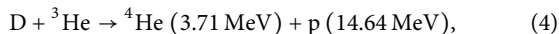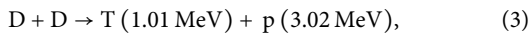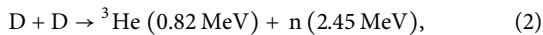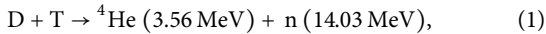
II. CHARGED PARTICLE MEASUREMENTS

Charged particle diagnostics span a broad range of measurements. In this section, some of the primary reactions and processes generating particles of interest are summarized, and information obtainable from the data is reviewed.

A. Reactions of interest

Sources of MeV ions in ICF and high-energy-density (HED) plasmas include primary fusion reactions, secondary fusion reactions, scattering reactions (frequently referred to as "knock-on" reactions), and laser–plasma interactions. "Primary reactions" is used as short-hand for reactions between ions originally in the fuel, while "secondary reactions" require two reaction steps: a primary reaction followed by reaction between one of its products and an ion originally in the fuel. (Similarly, tertiary reactions, where a product from a secondary step, in turn, reacts in a third reaction, are also possible but will not be discussed here.) Charged-particle-producing fusion reactions of key interest in an ICF/HEDP setting are

$$D + T \rightarrow {}^4He\,(3.56\,MeV) + n\,(14.03\,MeV), \tag{1}$$

$$D + D \rightarrow {}^3He\,(0.82\,MeV) + n\,(2.45\,MeV), \tag{2}$$

$$D + D \rightarrow T\,(1.01\,MeV) + p\,(3.02\,MeV), \tag{3}$$

$$D + {}^3He \rightarrow {}^4He\,(3.71\,MeV) + p\,(14.64\,MeV), \tag{4}$$

$$T + {}^3He \rightarrow {}^4He\,(4.80\,MeV) + D\,(9.52\,MeV). \tag{5}$$

$$T + {}^3He \rightarrow {}^4He + p + n + 12.1\,MeV. \tag{6}$$

Here, D represents deuterons, T represents tritons, p protons, and n neutrons. The energies given are the nominal birth energies assuming zero-energy reactants. This list is not exclusive; the diagnostic suite described in this paper has, for example, also been used to measure the fusion products from T + T reactions[11] and ${}^3He + {}^3He$ reactions,[12] and can be adapted to study other reactions as well. The total number of reactions of each type, henceforth referred to as yield, is obtained by integrating the product of the densities of the reactants and the reactivity over space and time as

$$\iint \frac{n_i n_j}{1 + \delta_{ij}} \langle \sigma v \rangle_{ij}\,dV dt, \tag{7}$$

where δ is the Kronecker delta and ⟨σv⟩ the reactivity, which in turn can be calculated as

$$\langle \sigma v \rangle = \iint f(\vec{v}_i) f(\vec{v}_j) \sigma(|v_{rel}|)|v_{rel}|\,d\vec{v}_i d\vec{v}_j, \tag{8}$$

where $f(\vec{v}_{i(j)})$ is the ion velocity distribution, σ the cross section, and v_{rel} the relative velocity of the two reacting ions. Assuming Maxwellian ion velocity distributions, the reactivities for each of the reactions can be calculated as a function of plasma ion temperature (T_{ion}), with the result shown in Fig. 1. Here, the reactivities for reactions (1–4) are obtained using the parameterization from Ref. 13, while the reactivity for reaction (5) is calculated based on the cross section from ENDF/B-VII.0. As can be seen, the reactivity depends strongly on the reaction type.

A secondary reaction of particular importance in the context of charged particle diagnostics happens when a ${}^3He$ ion born in reaction (2) reacts with a D ion originally in the fuel according to reaction (4) before losing its full birth energy. Since ${}^3He$ ion will have an energy ≤0.82 MeV, the fusion products from this secondary reaction will span a much broader range of energies than fusion products from a primary reaction, with proton energies ranging from 12.6 to 17.5 MeV and alpha energies from 6.6 to 1.7 MeV.[14] The yield of secondary reactions will be down by orders of magnitude compared with primary reactions, due to the much lower densities of the reactants in this case.

Key scattering reactions of relevance in ICF involve elastic scattering (knock-on) of the 14-MeV neutrons born in reaction (1) on ions in the fuel or shell of an ICF target,

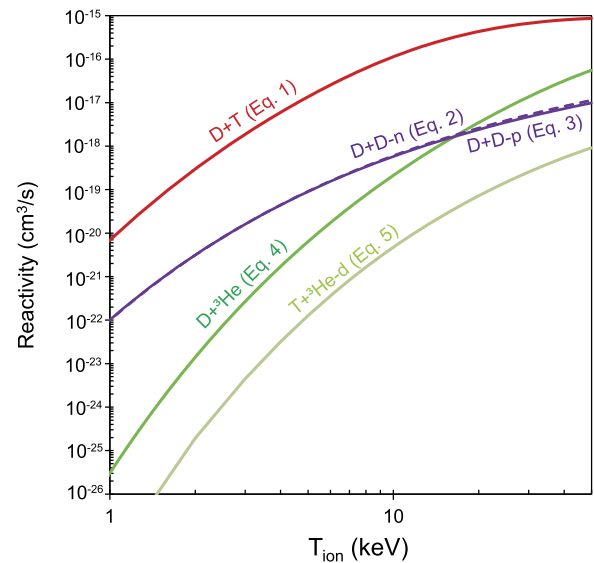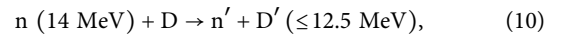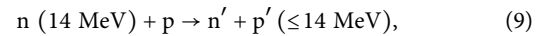$$n\,(14\,MeV) + p \rightarrow n' + p'\,(\leq 14\,MeV), \tag{9}$$

$$n\,(14\,MeV) + D \rightarrow n' + D'\,(\leq 12.5\,MeV), \tag{10}$$

FIG. 1. Reactivities for the charged-particle-producing reactions most commonly occurring in ICF/HED experiments.

$$n\,(14\,\text{MeV}) + T \rightarrow n' + T'\,(\leq 10.6\,\text{MeV}). \qquad (11)$$

Again, this is not an exclusive list; for example, neutrons from reaction (2) similarly also produce knock-on ions.[6]

The energy of the scattered ion depends on the scattering angle θ as

$$E_{ion'} = \frac{2A}{(1+A)^2}(1 - \cos\theta)E_n, \qquad (12)$$

where A is the ion mass number and E_n the initial neutron energy, resulting in broad emitted ion energy spectra given the 4π configuration typical of ICF implosions.

The final important source of MeV-range ions in ICF and HEDP experiments is laser–plasma interactions (LPI).[15] Two examples of LPI-generated MeV-range ions are considered here: ions intentionally generated using a short-pulse laser incident on a foil in the Target-Normal-Sheath-Acceleration[16,17] (TNSA) configuration, and "ablator" ions.[18] "Ablator" ions arise when the laser hits the ablator material surrounding a spherical ICF capsule. Laser light incident on a surface gives rise to a population of hot electrons through LPI. The fastest hot electrons escape the surface, resulting in a remaining space charge, which serves to accelerate ions off the surface material. These accelerated ablator ions typically follow an exponential energy spectrum, with the maximum energy determined by the potential on the surface,[19] which has been found to scale with laser intensity.[18] Ablator ions may be orders of magnitude more numerous than fusion products. In the context of this paper, they are mostly relevant as a background that has to be considered in the diagnostic design and preferably eliminated in order to obtain useful diagnostic data. At the NIF and OMEGA facilities, TNSA ions are generated using the OMEGA EP or NIF ARC short pulse laser beams and used as a probe beam for a subject plasma experiment (see Sec. IX).

B. Information in the charged particle emission

A significant amount of information about ICF implosions or HED plasma experiments is encoded in the charged-particle emission. On the most basic level, by counting ions with an instrument with a well-known efficiency, the reaction yield can be obtained. Frequently, the capability of separating contributions from different reactions is required; this is conveniently accomplished by using a magnet-based spectrometer (see Sec. V below) or Thomson Parabola (Sec. VI) and can also be accomplished by using CR-39 detectors (Sec. III C).

The ratio of scattering reaction[20,21] or secondary[14,22] yields to primary yields carries information about implosion ρR. As an example, for a plasma containing D, T, and hydrogen (H) in the fuel, assuming a hot-spot model for the implosion, the fuel ρR can be inferred from the ratio of the forward-scattered knock-on deuteron emission (Y_{KO-d}^{peak}) to the DT neutron yield emission (Y_n; Fig. 2) according to

$$\rho\langle R\rangle_{fuel} = \frac{\left(m_d + \frac{f_t}{f_d}m_t + \frac{f_h}{f_d}m_h\right)}{\sigma_{d,eff}}\frac{Y_{KO-d}^{peak}}{Y_n}, \qquad (13)$$

where $m_{d,t,h}$ are the ion masses for D, T, and H, $f_{d,t,h}$ the fractional content of D, T, and H in the fuel, and $\sigma_{d,eff}$ the effective cross-section for forward-scattered deuterons (~15.7% of the total n,D
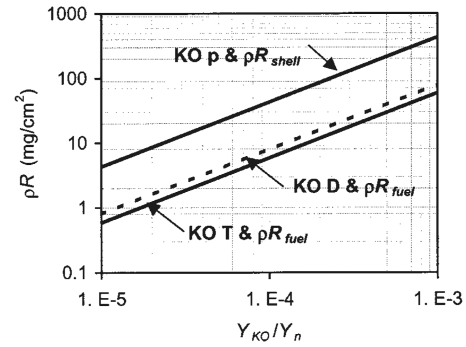
FIG. 2. Areal density (ρR) vs the ratio of knock-on particle yield to primary yield for knock-on deuterons (KO D) and tritons (KO T) and fuel ρR, and for knock-on protons (KO p) and shell ρR. Reproduced from Li et al., Phys. Plasmas **8**, 4902 (2001) with the permission of AIP Publishing.

elastic scattering cross section, or 100 mb).[20] The hotspot model represents a simplification of the expected implosion geometry; typically, a uniform model will more closely mimic reality, which leads to a factor 1.33 geometrical correction factor in Eq. (13) (Ref. 20).

FIG. 3. Ratio of secondary (Y_2) D³He-p (blue) and DT-n (red) yields to primary (Y_1) DD-n yields as a function of deuterium ρR. The Y_2/Y_1 ratio is linear up to a point but plateaus at higher compression at a level that depends on (a) plasma electron temperature (T_e) and (b) mix. Reproduced from Rinderknecht et al., Phys. Plasmas **22**, 082709 (2015) with the permission of AIP Publishing.

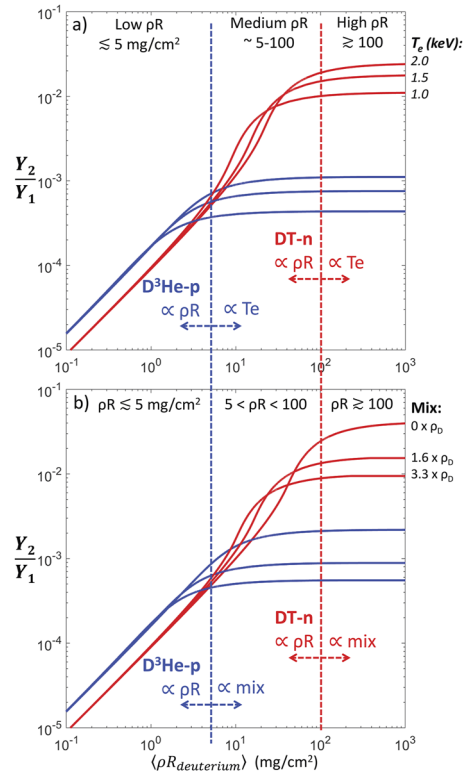Similarly, for a CH shell capsule, the shell ρR can be inferred from the knock-on proton emission (Fig. 2).

For secondary D^3He or DT (Ref. 23) fusion products, the ratio of secondary to primary yields depends linearly on ρR up to the point where the implosion is compressed enough for the ^3He born in reaction (2) or T born in reaction (3) to be completely stopped in the assembled plasma. At higher compression, the ratio plateaus at a level that depends on plasma electron temperature (T_e) and composition (mix; Fig. 3).[14,22] This level as well as the shape of the resulting fusion product energy spectrum also depends on plasma stopping power, and experiments have been undertaken to use this information to assess the validity of plasma stopping power models.[24]

Charged-particle energy spectra, including primary and secondary fusion product spectra as well as knock-on spectra, encode information about the plasma conditions traversed by ions born in the implosion on their way to a detecting spectrometer.[25] For a single spectrometer line-of-sight (LOS), this includes information about fuel and shell ρR, manifested as downshift and broadening of birth energy spectra,[25,26] and about any remaining electric field due to charging of the capsule from laser interaction, manifesting as energy upshifts.[25,27,28] With multiple spectrometer LOS, energy spectra measurements also provide key information about ρR symmetry.[26,29,30] The maximum ρR that can be measured using this technique depends on the ion species studied and on the ion birth-energy; at sufficiently high ρR, ions will be stopped in the converged implosion and, thus, unable to reach the detecting instruments. As an example, the shape of KO-d energy spectra can be used to infer ρR from cryogenically layered DT implosions up to an upper limit of ~200 mg/cm^2 (Ref. 31). Using D_2 and ^3He gas in the implosion fuel fill produces primary 14.7 MeV protons and maximizes the implosion ρR diagnosable using charged-particle techniques. This method has been frequently employed to diagnose surrogate implosions at the NIF,[32,33] and can be used to differentially diagnose shock and compression ρR,[34,35] with the shock emission peak appearing at higher energy than the subsequent compression peak (Fig. 4).

For low-ρR, shock-driven implosions, avoiding charged-particle energy upshifts due to capsule charging is key to allowing the diagnosis of implosion ρR. This is optimally achieved by keeping the laser intensity below the threshold for hot-electron generation,[19] or by ensuring that the implosion burns significantly after laser turn-off,[28] allowing any fields generated from hot-electron generation to decay before the charged-particles are emitted. Inferring ρR from measured spectra requires assumptions about plasma density and T_e as well as a model for plasma ion stopping. Conversely, with well-diagnosed plasma conditions, measured charged-particle energy spectra have also been successfully used to constrain theoretical modeling of plasma stopping power.[36,37] In addition to ρR information, charged-particle spectra also encode information about plasma ion temperature[38] (T_{ion}) and non-thermal plasma flows,[39] analogously to information obtained from neutron spectra.[40–42] However, in practice, the effects of ion energy loss due to ρR and upshifts due to any remaining fields during particle emission make it extremely challenging to obtain such information from charged-particle spectra with any accuracy.

Measurements of the time-dependence of the charged-particle emission provide information about the timing of fusion reactions relative to the onset of the laser (bang time) and the reaction history, including differential shock and compression bang times where applicable (Fig. 4). These measurements are similar, and frequently compared, to neutron and x-ray emission history data obtained with diagnostics such as the Neutron Temporal Diagnostic[43] (NTD) on OMEGA (Fig. 4) or the Streaked Polar Instrumentation for Diagnosing Energetic Radiation[44] (SPIDER) at the NIF.
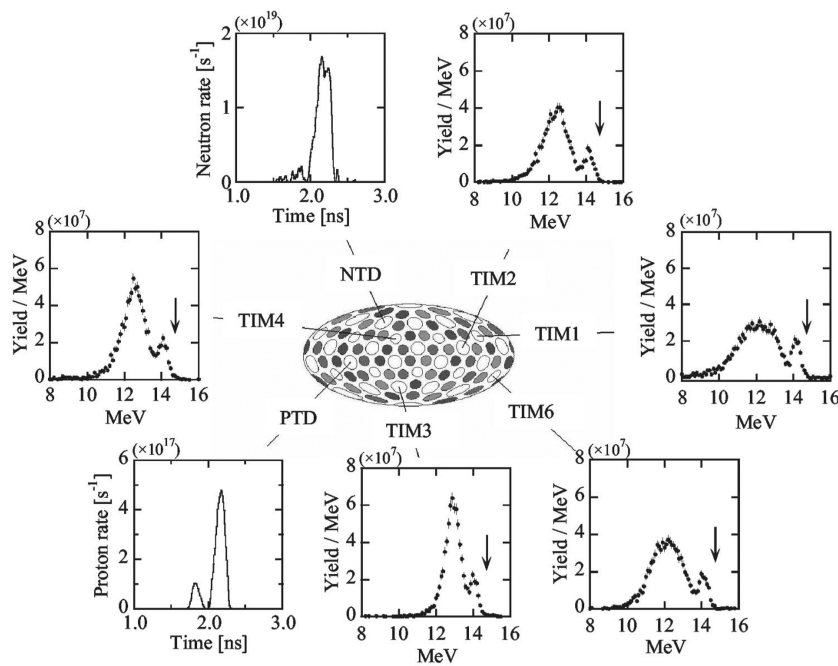
FIG. 4. Example D^3He-proton energy spectra (TIM1, TIM2, TIM3, TIM4, and TIM6) and proton (PTD) and DD-neutron (NTD) emission histories as measured in different LOS from OMEGA implosion 31271. The energy spectra clearly display both shock-emission (high-energy) and compression-emission (low-energy) protons, which can be differentially analyzed to infer ρR at both times (the birth-energy is indicated with arrows). Similarly, the PTD data also show shock (early time) and compression (late time) peaks, allowing the relative timing of the two implosion stages to be inferred. The multiple LOS allows the study of implosion symmetry. Reproduced from Frenje et al., Phys. Plasmas **11**, 2798 (2004) with the permission of AIP Publishing.

The charged-particle emission can also be imaged to obtain a spatially resolved picture of the implosion. To obtain sufficient statistics in the images, this is mostly done using penumbral imaging techniques.[45] Imaging in multiple LOS[46] allows tomographic reconstruction of implosion shape.

As will be discussed in Sec. IX, charged particles can also be used as a probe (backlighter) to assess conditions in a subject plasma. In this case, the source of ions can be a shock-driven implosion (mono-energetic backlighter) or TNSA. Yield, timing, and spectrally resolving charged-particle diagnostics are frequently applied also in this scenario, but the most important diagnostic, in this case, is typically a flat imaging detector recording the source ions after transmission through the subject plasma, allowing analysis of electric and magnetic field and density fluctuation effects on the probe ions.

Finally, the suite of charged-particle diagnostics can also be applied for basic science experiments, including nuclear physics experiments relevant to nuclear astrophysics.[47] Ground-breaking experiments using the HEDP platform[11,48] to study nuclear astrophysics-relevant nuclear reactions in a stellar-like environment include measurements of T^3He (Refs. 12 and 49) and $^3He^3He$ (Ref. 12) fusion products.

C. Dynamic range and energy bite considerations

HEDP and ICF experiments span a broad range of charged particle yields and include ions over a broad range of energies [Eqs. (1)–(6), (9)–(11)]. Diagnostics for charged particle emission are designed to optimally cover a broad range of yields and ion energies. As an example, Fig. 5 (Ref. 50) illustrates the coverage of existing OMEGA and NIF CR-39-based spectrometers for proton measurements. Higher yield applications, including TNSA, typically require use of a different detector material, e.g., radiochromic film (RCF) or image plates (IP), such as used for the electron-positron-particle spectrometers (EPPS) described in Sec. V A.

III. DETECTORS FOR TIME-INTEGRATED MEASUREMENTS

Passive detectors are used as the recording medium for time-integrated measurements in a large number of charged-particle diagnostics applications for HEDP and ICF. They share the common advantages of high intrinsic spatial resolution and insensitivity to electric and magnetic pulses from the harsh laser interaction environment, which lead to them being preferable to electronic detectors in many cases.

A. Image plates

Image plates[51] (IP) are commonly used for ICF and HEDP experiment x-ray detection.[52–55] They are also sensitive to particle radiation; in terms of charged-particle diagnostics, they have been primarily used with the electron-positron-proton spectrometers[56] (EPPS, Sec. V A) and Thomson Parabola[57] detectors (Sec. VI). An IP consists of a plastic backing plate coated with an active layer of photostimulable phosphor crystals with an Eu^{2+} dopant. Incident radiation ionizes the phosphor layer, generating Eu^{3+} ions and photoelectrons, creating electron–hole pairs. The IPs are designed so that
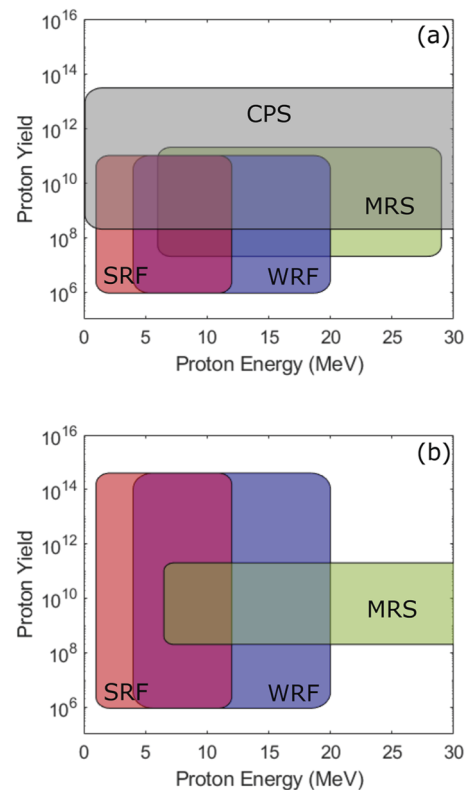

FIG. 5. Yield and energy range coverage for proton energy spectrum measurements using existing CR-39-based proton spectrometers at (a) OMEGA and (b) the NIF, including step-range filters (SRF) and wedge-range filters (WRF) described in Sec. IV, and the Charged Particle Spectrometers (CPS) and Magnetic Recoil Spectrometers (MRS) described in Sec. V. Reproduced from Lahmann *et al.*, Rev. Sci. Instrum. **92**, 083506 (2021) with the permission of AIP Publishing.

the electron–hole pairs are trapped in metastable states, temporarily storing information about the incident radiation. This information is retrieved post experiment using a dedicated image plate scanner, where a laser beam is used to photostimulate the metastable states; through this process, the electron–hole pairs recombine and produce light that is read out by a photomultiplier tube in units of photostimulated luminescence (PSL). The exposure/readout process is illustrated in Fig. 6.

IPs are erased when exposed to light, and can be reused in multiple experiments. The intensity of the IP response decays as a function of time post exposure;[54,55] the decay curve can be characterized, and the (energy-dependent) response of IPs to radiation calibrated relative to a known source emission to facilitate absolute measurements.[54–58]

B. Radiochromic film

Radiochromic film[59] (RCF) is an ambient-light-safe film material sensitive to ionizing radiation, including x-rays and charged-particles. The material consists of one or two thin, proprietary active layers of organic microcrystal monomers embedded in polyester. The film turns a shade of blue when exposed to ionizing radiation,
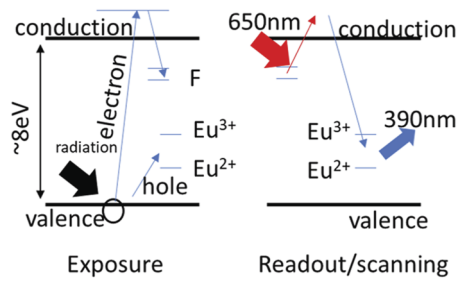
FIG. 6. Schematic illustrating the ionizing radiation detection principle for FUJI BAS SR type IP detectors with a BaFBr:Eu^{2+} active layer. Incident radiation ionizes the Eu^{2+} dopant and creates electron–hole pairs that are trapped in a metastable state. The electron–hole pairs are stimulated to recombine using a laser beam during the readout/scanning stage. Reproduced from Holder *et al.*, Rev. Sci. Instrum. **89**, 10F123 (2018) with the permission of AIP Publishing.
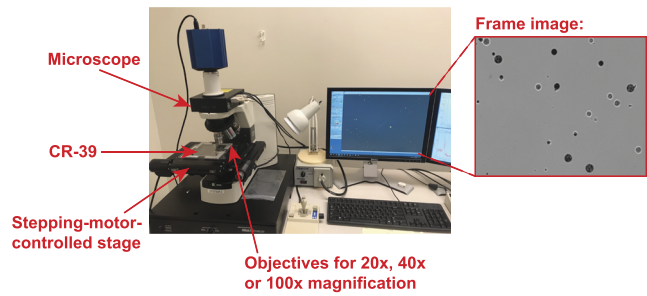

FIG. 7. Setup for scanning CR-39. The system steps across the CR-39 surface, analyzing each microscope frame (example shown in inset) for tracks. For each detected track, contrast, eccentricity, diameter, and position are recorded.

and requires no development. Some increased dyeing of the film is observed within the first 24 h of exposure (on the level of 10% intensity[60]); the recorded image subsequently remains stable over a timescale of months. The spatial resolution of the film is better than 2.54 μm.[60]

In the context of HEDP and ICF charged-particle diagnostics, RCF is primarily used for TNSA proton imaging, where it is typically fielded in the form of a stack with the multiple layers optimally sensitive to protons of different energies.[61,62] Typically, RCF results are recorded by scanning the film post-experiment using a regular film scanner. A microdensitometer can also be used to obtain precise measurements of optical density (OD) across the film. The OD can then be converted to dose, which is proportional to the incident flux of ionizing radiation, allowing absolute measurements of particle flux.

C. CR-39

CR-39 solid-state nuclear track detectors[63] (chemical composition $C_{12}H_{18}O_7$) have been used for ICF and HEDP applications since at least the early 1980s.[64–66] Each ion incident on the CR-39 surface will generate a trail of broken molecular bonds, which can be developed into a micron-scale track visible under an optical microscope through etching in hot NaOH. In comparison to IPs and RCF, CR-39 detectors provide the dual advantages of being insensitive to x-rays and electrons and having the capability to separate tracks generated by different ion species.[6,67] On the other hand, CR-39 dynamic range is limited by the requirement that individual particle tracks remain spatially separated on the detector surface[68] (although for some applications, this can be extended by opacity analysis[69]).

Contemporary CR-39 processing techniques involve etching the materials in NaOH at 80 °C for 0.5–6 h, depending on track fluence and particle type studied, to develop the charged-particle-induced tracks. Post-etching, the detectors are scanned using auto-focusing optical microscopes and a stepping-motor-controlled stage (Fig. 7), allowing piece-wise rectangular images of order 0.1–1 mm^2 area to be recorded across cm-scale pieces of CR-39. For each image, the custom-written scanning software automatically identifies tracks on the CR-39, and records their properties in terms of a darkness

(contrast, typically calculated in units of track brightness divided by background brightness), roundness (eccentricity), size (diameter), and position (x, y). Ions with normal incidence on the CR-39 typically produce round tracks, with size and darkness depending on ion species and energy.

Ions will penetrate as deep into the CR-39 as their incident energy allows. Along their range, track size will increase monotonically with the etch time and local stopping power of the particle, where the stopping power depends on the particle's energy, charge, and mass.[70] Tracks start out faint at short etch time and/or high particle energy, become darker and larger at lower energy and/or longer etch time, and then again fainter and smaller as the etch depth approaches the end of the track. This behavior is illustrated in Fig. 8 for protons with energies ranging from 9.2 MeV (barely developed in the upper left corner) to 1.1 MeV (faded at the end of
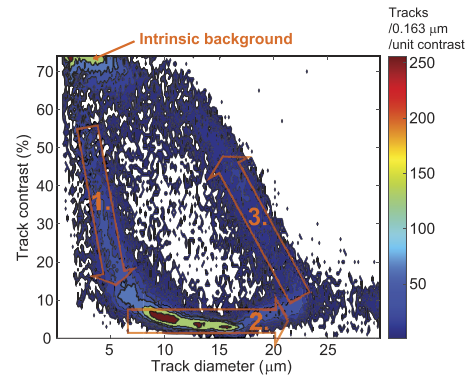

FIG. 8. Background-subtracted contours of track contrast vs diameter on a piece of CR-39 exposed to protons with energies from 1.13 to 9.18 MeV, etched for 6 h in 6-M NaOH at 80 °C, and scanned with 40× magnification. Contrast is calculated as track brightness divided by background brightness; hence, the lowest contrast numbers correspond to the darkest tracks. Typically, intrinsic noise in the CR-39 appears primarily in the upper left in this space (small, faint tracks). Signal tracks will develop from small/faint in the upper left corner at short etch time and high energy (arrow 1) to larger and very dark with increased etch time and lower energy (arrow 2) and then gradually fainter and smaller again as the tracks are etched out (material removed approaches the depth of the formed track on the CR39, arrow 3). Note that the absolute scale is in units of tracks/bin and will depend on track density on the piece of CR-39 scanned.
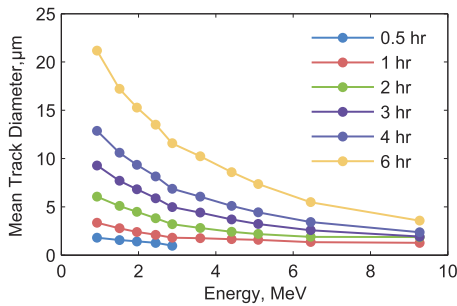
FIG. 9. Mean proton track diameter as a function of energy inferred at etch times (in NaOH at 80 °C) ranging from 0.5 to 6 hours. Reproduced from Sinenian *et al.,* Rev. Sci. Instrum. **82**, 103303 (2011) with the permission of AIP Publishing.
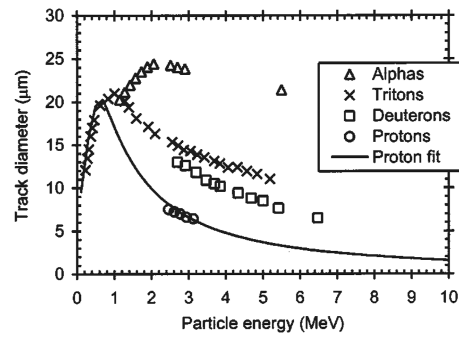

FIG. 10. Track diameter as a function of particle energy (DvE) for light ion species commonly detected in ICF and HEDP applications. Reproduced from Séguin *et al.,* Rev. Sci. Instrum. **84**, 975 (2003) with the permission of AIP Publishing.

the No. 3 arrow) at a fixed 6 h etch time in NaOH at 80 °C. Similarly, Fig. 9 (Ref. 71) shows how proton tracks grow with etch time and reduced energy; other ion species will follow a similar pattern but with different maximum track diameter due to their different local stopping power.[6,70] Given an understanding of the incident particle energy range, different ion species can be separated based on their track size on the CR-39 (Fig. 10, Ref. 6). Note that while Figs. 8–10 illustrate "typical" track development, the exact track behavior as a function of energy and etch time will vary between individual pieces of CR-39.[70,72]

Typically, 100% detection efficiency can be assumed for particles in the lower half of Fig. 8; for ions that fall in the upper left, some efficiency will be lost due to underdeveloped tracks, and for ions in the upper center-right, efficiency will be gradually lost due to over-etching. This means that to ensure 100% detection efficiency, any detector setup using CR-39 must be optimized to allow long etch times (limited particle fluence[68]), and for the energy of the ions when incident on the CR-39 to fall in the intermediate energy range (typically, ~1–4 MeV).[70] The energy-on-CR-39 is typically optimized through the use of, e.g., Aluminum, Tantalum, or mylar overlay filters that slow the incident particles into the optimal range before detection on the CR-39 surface.

The primary backgrounds that impact charged particle detection using CR-39 are intrinsic background, due to defects in the CR-39 itself, and neutron-induced background. Neutrons can interact with CR-39 through elastic or inelastic scattering or nuclear reactions, generating energetic ions that leave tracks in the CR-39. The probability for neutron interactions leaving behind observable tracks has been empirically determined to be $(1.1 \pm 0.2) \times 10^{-4}$ for DD neutrons and $(6.0 \pm 0.7) \times 10^{-5}$ for DT neutrons (Fig. 11; Ref. 73). Levels of intrinsic background observed in CR-39 can vary substantially from piece to piece, and with the track contrast limit required in the analysis (Fig. 12, Ref. 74). Typically, with optimal etch conditions and particle energies, most intrinsic noise can be effectively eliminated from the signal by appropriate contrast and diameter cuts in the analysis (Fig. 8).

Both neutrons and intrinsic noise generate tracks with a wide distribution of eccentricities (roundness). Typically, charged-particle applications will be designed to have ions normally incident on the CR-39 to ensure round tracks, for maximum detection efficiency as well as maximized ability of separating signal from noise based on track eccentricity. However, certain applications may require CR-39 to be fielded at an angle. Progressively larger angles of incidence lead to more eccentric tracks, with lower energy ions being etched out faster and higher energy ions developing more slowly; operation with an angle of incidence ≥30° off from normal has been shown to lead to substantially reduced efficiency.[74]

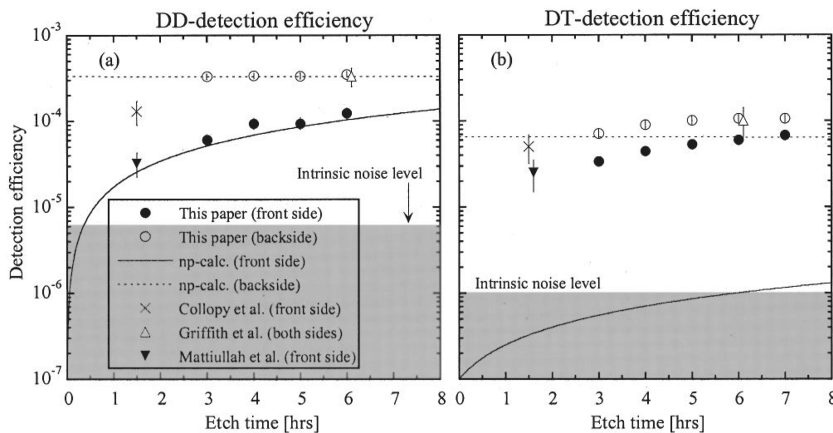**FIG. 11.** Experimentally determined CR-39 neutron detection efficiency for (a) DD and (b) DT neutrons. Neutrons interacting in CR-39 generate ions through elastic and inelastic nuclear reactions, leaving behind tracks that appear as a background to be handled in charged-particle applications. Reproduced from Frenje *et al.*, Rev. Sci. Instrum. **73**, 2597 (2002) with the permission of AIP Publishing.
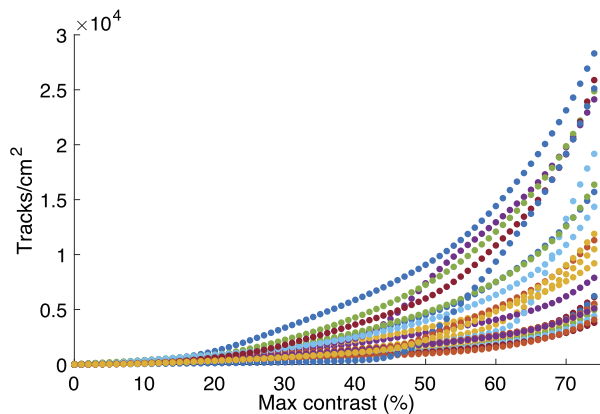
FIG. 12. Intrinsic noise density as a function of max track contrast considered in the analysis, experimentally determined for a number of different pieces of CR-39 (different colors) not exposed to ions. Reproduced from Przobocki *et al.*, Rev. Sci. Instrum. **92**, 013504 (2021) with the permission of AIP Publishing.

While CR-39 is generally insensitive to x-rays, exposure to a significant x-ray dose has been found to reduce the size of developed tracks.[75,76] Further studies are under way to quantify this effect for applications using track size on CR-39 for inference of incident particle energy (Sec. IV). Prolonged (>16 h) exposure to vacuum prior to irradiation has also been found to reduce effective track size on the CR-39.[77]

IV. CR-39 TRACK-SIZE-BASED SPECTROMETERS

The simplest type of charged-particle spectrometer for ICF and HEDP applications uses metal filter(s) in front of a piece of CR-39, relying on the energy-dependence of track size on the CR-39 to infer the incident ion energy spectrum. Such spectrometers can conveniently be made very compact (typically $\phi = 5$ cm), enabling fielding in many different LOS around the OMEGA or NIF target chambers as well as close to the experiment for high detection efficiency. At OMEGA, six ten-inch manipulators (TIM) and one nuclear diagnostic inserter (NDI) can currently be used to field these detectors at distances ranging from 10.5 to 175 cm from the implosion (Fig. 4). At the NIF, four different diagnostic insertion manipulators (DIM) can each field up to four of these detectors at ∼50 cm from the implosion, with some having the additional capability to field detectors at 10 cm from the implosion (Fig. 13). In principle, the DIMs can also be retracted to field the detectors at a selected further removed standoff-distance up to ∼700 cm, but this is challenging because DIMs are mostly used to field more than one diagnostic, with the compact spectrometers run in "add-on" mode.

A. Step-range filters (SRF)

Because of variations in the CR-39 track diameter-vs-energy (DvE) response between different pieces of CR-39 as well as due to variations in ambient conditions such as x-ray or vacuum exposure as discussed in Sec. III C, fielding the CR-39 with a single, flat metal filter is not sufficient to accurately infer the energy spectrum.
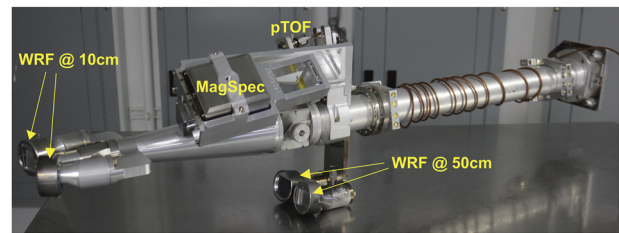

FIG. 13. Diagnostic insertion manipulator (DIM) front-end with charged-particle diagnostics as fielded on the NIF. This snout holds four compact wedge-range-filter (WRF) spectrometers at 10 cm and 50 cm from the implosion, the particle time-of-flight detector (pTOF), and a compact magnet-based spectrometer (MagSpec). The snout is simultaneously also used for imaging (hardware inside the tube).

The simplest CR-39-based spectrometer uses a number of flat filters of varying thickness in a step-range-filter (SRF) configuration. The energy spectrum from these detectors can be crudely inferred by counting ions behind each filter and comparing what fraction of ions penetrated each thickness; assuming some of the filters are thick enough for the ions to be stopped in the filter before reaching the CR-39, their energy can be inferred.[78] However, this method only works for peaked incident energy spectra, and is complicated by the fact that the low-energy cut-off for 100% CR-39 detection also varies with etch time and piece of CR-39. A better analysis method is to vary the DvE response within a known parameterization until the measured diameter distributions behind each filter thickness line up in energy space. This method has been found to work well for reconstructing energy spectra of arbitrary shapes, albeit with limited energy resolution.[50] A major advantage of the SRFs is that they can be made arbitrarily thin, with the low-energy cut-off for detection primarily determined by the maximum energy of ablator ions expected from an experiment (due to their high fluence, ablator ions will overwhelm any signal ions if they are allowed to penetrate the filters[79]). Because of the compact size and flexible fielding arrangements of the SRFs, they also span a broad range of particle yields (Fig. 5). However, in practice, SRFs are only useful for measuring protons and higher-energy deuterons; filters thin enough to allow measurement of alpha particles will inevitably be penetrated by ablator protons, overwhelming any alpha signal.

B. Wedge-range filters (WRF)

The workhorse CR-39 track-size-based spectrometer is the wedge-range-filter (WRF), which has been in frequent use since 2001.[6,72] In this application, a wedge-shaped filter with a minimum of two fiducial holes is fielded in front of the CR-39, and the energy spectrum inferred based on track size vs position behind it (Fig. 14).

The thickness of the wedge is calibrated as a function of position using D^3He protons of known energy generated using a linear electrostatic ion accelerator at MIT (Fig. 14),[80] allowing the DvE parameterization and, subsequently, incident energy spectrum to be inferred from track size vs position data. The WRF most frequently used is made of Aluminum and fits in a $\phi = 5$ cm can for fielding; smaller versions and other materials have been tried as well.[72] WRFs are typically limited to a low proton-energy cut-off ≥4 MeV (Fig. 5) due to challenges in machining thinner wedge filters.
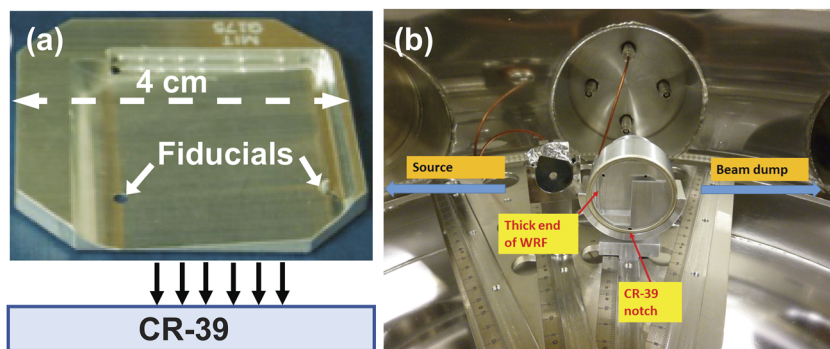
FIG. 14. (a) Picture of a standard Aluminum wedge-range-filter (WRF), illustrating the detection principle: track size is measured as a function of position on the CR-39, and used to infer the incident energy spectrum based on the calibrated thickness vs position (relative to the fiducials) of the WRF. (b) Prior to use, each WRF is individually calibrated using D^3He protons at two (nominal and reduced through the use of an overlay filter) energies at an MIT accelerator.

V. MAGNET-BASED SPECTROMETERS

Magnet-based charged-particle spectrometers use magnetic dispersion to spatially separate ions of different energies, with the incident energy spectrum reconstructed from the resulting intensity vs position measurement. The position at which the ions are detected is determined by their gyroradii R_{gyro} through the magnetic field, where R_{gyro} depends on ion charge, mass, and energy according to

$$R_{gyro}^2 \propto \left(A/Z^2\right)E, \tag{14}$$

where A is the ion mass number, Z the charge number, and E energy. Charged-particle magnetic spectrometers in a Rutherford-scattering geometry were used in the SNL intense ion beam ICF program, using time-integrating CR-39 detectors in conjunction with time-resolving p-i-n diode detectors.[65,81,82]

Four time-integrating magnetic spectrometer types with varying characteristics are currently in use at the NIF and/or OMEGA: the electron-position-proton spectrometers (EPPS), the charged-particle spectrometers (CPS), the magnetic recoil spectrometer (MRS; more commonly known as a neutron spectrometer[83,84]), and the recently implemented compact magnetic spectrometer (MagSpec). Each is briefly described in this section.

A. Electron-position-proton spectrometer (EPPS)

The electron-position-proton spectrometers (EPPS) (Ref. 56) are compact, adaptable instruments using permanent Neodymium dispersion magnets. They have historically been used with IPs, RCF, a charged-coupled device (CCD),[85] or scintillating fiber[86] as the detector; IP is the detector type used at OMEGA EP and the NIF.[87,88] The NIF (Fig. 15) and OMEGA EP implementations can be fielded in different DIMs and TIMs, allowing measurements of directional spectra. EPPSs have also been frequently fielded on short-pulse laser systems.[56]

The use of IPs as the detector allows the detection of electrons and positrons as well as ions; the absolute calibration of IPs for electrons with energies 0.1–4 MeV has been determined to allow spectral measurements.[89] The dispersion of the system has been calibrated for both protons[87] and electrons.[88]

In terms of proton spectrum measurements, EPPS is frequently used to diagnose the high-intensity, high-energy spectra generated in short-pulse laser interactions using NIF-ARC or OMEGA-EP;

the image plate detectors allow measurements of much higher incident proton fluences compared with CR-39 detectors. Magnets with varying field strength allow for different energy coverage options; depending on the magnet choice, EPPS on NIF can measure protons from 0.5 to 100 MeV. Using a magnet with lower field strength and reduced energy coverage allows for measurements with improved energy resolution.

B. Charged-particle spectrometer (CPS)

Two versatile charged-particle spectrometers (CPS1 and CPS2) have been in use at OMEGA for the past two decades.[6,90] These instruments each consist of a 5.6 kG permanent bending magnet, a selectable-size slit used to vary efficiency to allow operation over a broad range of yields (Fig. 5), an array of CR-39 detectors covering a broad range of energies with overlay filtering designed for optimal detection of low-Z ions, including p, D, T, ^{3}He and α, and an x-ray reference finger used to record an image of the slit used on an experiment for verification purposes. The CPSs are fielded in fixed locations at OMEGA, with the CPS1 slit (after a recent relocation) fielded 255 cm from the target chamber center (TCC) in port H11, and the CPS2 slit 100 cm from TCC in port H1. The setup for CPS1 is illustrated in Fig. 16; the CPS2 detector design is nominally the same, but the system is fielded inside the OMEGA target chamber, necessitating a different support structure and slit design.

Resolution in the measurement varies with particle energy and slit width used. For example, with a 0.2 mm wide slit the full-width half maximum (FWHM) resolution for 3 MeV protons is
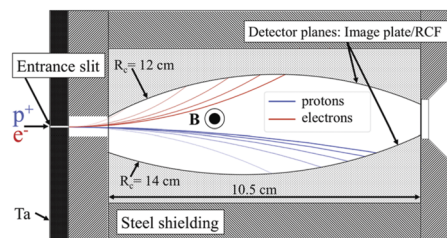

FIG. 15. Schematic of the NIF EPPS. Charged particles (electrons, positrons, or ions) enter the magnet through the slit on the left, are momentum-separated in the permanent magnet, and detected using IPs or RCF in the detector plane. Reproduced from Mariscal *et al.*, Rev. Sci. Instrum. **89**, 10I145 (2018) with the permission of AIP Publishing.
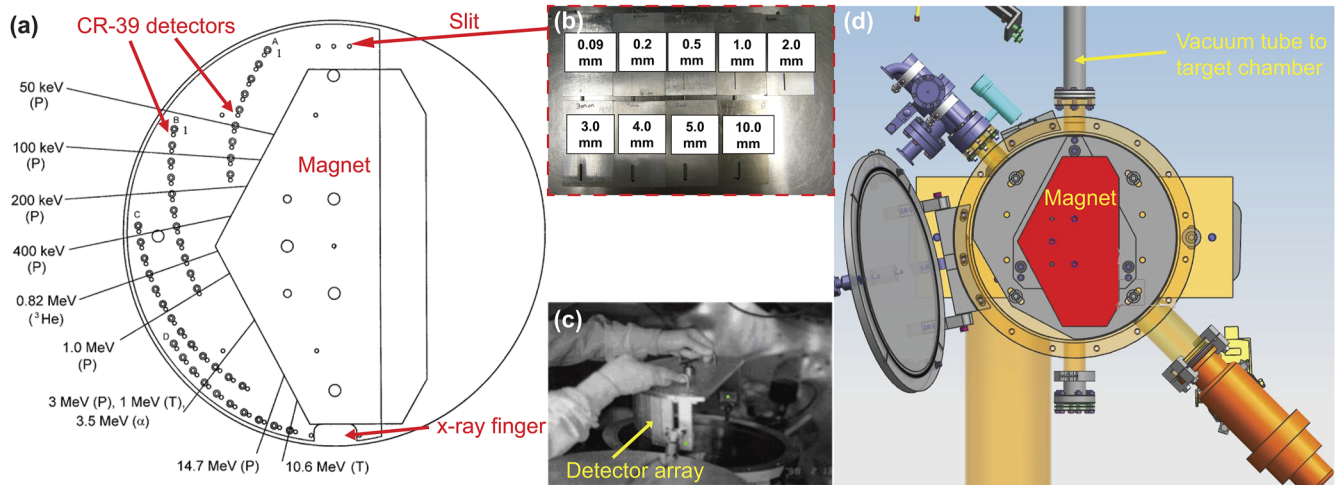
FIG. 16. (a) Schematic of one of the OMEGA charged-particle spectrometers (CPS1), which uses a permanent 5.6 kG magnet, selectable-width slits (b), and CR-39 detectors to measure low-Z ion spectra over a broad range of energies (0.1–30 MeV for protons). Panel (c) shows a picture of the detector array, and (d) a model of the setup indicating orientation relative to the OMEGA target chamber.

extremely good at ~10 keV, while with a 2 mm wide slit the resolution for 14.7 MeV protons is poor at ~1.1 MeV. Knowledge about CR-39 track-size vs energy (Fig. 10) is used to discriminate contributions from different ions in the same position on the detector array, allowing simultaneous detection of multiple ion species.[6,70]

The CPSs are workhorse detectors used to infer ρR for ICF implosions,[20,31,91,92] and they provide unique data for basic science experiments on the HEDP platform, including nuclear experiments[12,93] and stopping power experiments.[36,37]

C. Magnetic recoil spectrometer (MRS)

Similar to CPS, the magnetic recoil neutron spectrometers (MRS) also use an aperture in front of a permanent magnet with a CR-39 detector array. The MRSs are neutron spectrometers routinely used to infer yield, T_{ion}, and ρR from DT implosions at OMEGA and the NIF,[83,94–96] but they can be straightforwardly reconfigured to operate CPS-style by fielding them without the CD conversion foil required to convert neutrons to deuterons for detection (Fig. 17). Unlike CPS, the MRS uses a focusing magnet, which allows for a much larger aperture to be used, increasing efficiency without loss of resolution. The NIF MRS uses a fixed aperture with area A_{ap} = 2 × 10 cm^2 at 596 cm from TCC, while the OMEGA MRS can be configured to operate with A_{ap} = 2 × 11 cm^2, A_{ap} = 1 × 11 cm^2, or A_{ap} = 2 × 1 cm^2 225 cm from TCC. The apertures are tilted 14.2° to attach to the magnet, for a total charged particle detection efficiency ε of

$$\varepsilon = \frac{A_{ap} \times \cos14.2°}{4\pi d^2}, \quad (15)$$

where d is the aperture stand-off distance. To ensure normal incidence of the ions onto the CR-39 detectors, these are tilted relative to the focal plane, leading to variations in energy resolution from ~0.1 to 0.4 MeV in charged-particle mode across the CR-39 pieces

and the range of detectable energies. Similar to CPS, charged-particle mode MRS can also be used to measure ρR on ICF implosions,[97] and for basic science measurements, including nuclear physics experiments.[11,12,48]

D. Compact magnet spectrometer (MagSpec)

As can be seen in Fig. 5, there has been limited capability available at the NIF to measure low-energy ions at low yields. The SRFs, which provide some capability to measure the proton spectrum below 4 MeV, have limited resolution, limited ability to field on indirect drive implosions due to concerns about hohlraum debris damaging the filters, and cannot measure other ion species of interest, e.g., alpha particles. The compression proton spectrum from indirect drive D^{3}He-gas-filled implosions at the NIF will include protons below the WRF low-energy cut-off of 4 MeV,
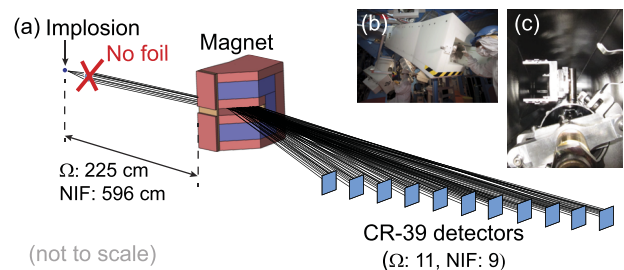

FIG. 17. (a) Schematic of MRS runs in charged-particle configuration, without the CD conversion foil used in neutron spectrometry mode. Both the NIF and OMEGA MRS systems use an aperture in front of a permanent Nd-Fe-B focusing magnet and an array of CR-39 detectors (9 on the NIF, 11 on OMEGA) covering deuteron energies from ~3 to 20 MeV. (b) Picture of the OMEGA MRS detector tube inside its shielding and (c) CR-39 detector array inside the detector tube.

and accurate measurement of proton yield (used for, e.g., D^{3}He cross section measurements[98]) and energy (used to infer compression ρR[32]) requires measurement of lower-energy protons. The capability to measure alpha particles will enable further nuclear astrophysics-relevant experiments using the direct-drive NIF platform.[99] For these reasons, another CPS-like magnet spectrometer system, MagSpec, intended to be fielded attached to the side of a DIM for in-close, high-efficiency operation, was recently implemented (Fig. 13, Ref. 101). Similar to CPS, this compact system also uses a permanent bending magnet with a slit in front and with CR-39 as the detector. MagSpec has also been adapted for fielding in a TIM on OMEGA. Analysis methods for this new capability are under development.

E. Calibration of the magnetic dispersion

For accurate energy spectrum measurements, the energy vs position axis of the magnetic spectrometers must be calibrated.[87] Methods developed for this include off-line calibration with source ions of known energy,[87] and *in situ* calibration using a fusion source.[83] The former method relies on setup parameters, including alignment of the system, being maintained between the off-line tests and fielding on an experiment, and the latter, which typically involves cross-calibration to another detector fielded on the same experiment, relies on the assumption that the fusion source emission energy is uniform around an experiment. This will not hold true in case of ρR asymmetries or directional flow. An alternative method, aligning an alpha-emitting radioactive source in the target chamber for *in situ* calibration using ions of known energy, has been recently developed and is now available at OMEGA.[101]

VI. THOMSON PARABOLA

In standard magnet-based spectrometers, ions with the same (A/Z^2) will overlap at the same position [Eq. (14)]. While at moderate fluences, overlapping ions can be separated based on their DvE on CR-39 detectors, for some applications, such as at very high ion fluences, it is advantageous to use the Thomson Parabola (TP) technique.[102] With TP, an electric field is added parallel to the magnetic field, and ions are simultaneously magnetically and electrically dispersed along parabolas of constant Z/A over a 2D surface, allowing spatial separation of species with overlapping (A/Z^2). In the HEDP field, TP methods were first developed for short-pulse laser applications (see, e.g., Refs. 103–107).

A Thomson Parabola Ion Energy analyzer[57,108] (TPIE) was developed for use at OMEGA and OMEGA-EP (Fig. 18). This versatile instrument consists of a square pinhole in front of a permanent dipole magnet and electrode and is fielded in a TIM at either facility, with distance to TCC, pinhole size, and strength of the magnetic and electric fields adjustable to optimize for different applications. Three magnets with field strengths of 1.6, 5.6, and 8.4 kG are available for selection. The system is fielded with CR-39 or IP detectors, depending on the application (CR-39 for absolute fluence measurements, IP for high-fluence applications). On OMEGA EP, TPIE is typically used to measure the high-intensity ion spectra from TNSA.[109–111] On OMEGA, TPIE has been successfully used to measure spectra of ablator ions,[19] and ions accelerated in fast-ignition experiments.[112]
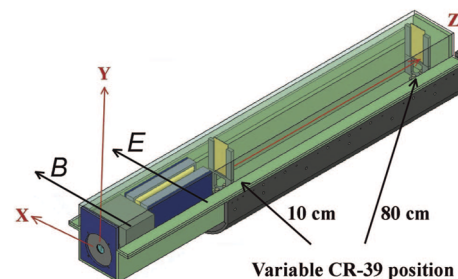

FIG. 18. Schematic of the Thomson Parabola Ion Energy analyzer (TPIE) in use at OMEGA and OMEGA-EP. Reproduced from Cobble *et al.*, Rev. Sci. Instrum. **82**, 113504 (2011) with the permission of AIP Publishing.

VII. SPATIAL PROFILE MEASUREMENTS

Similar to techniques used for neutron imaging (see Ref. 10 and references therein), imaging of the charged-particle spatial emission profile can be used to reconstruct the shape of the burning plasma source. The capability of imaging protons from the D^{3}He and DD reactions was introduced on OMEGA about two decades ago in the form of the Proton Core Imaging System (PCIS),[45,113] using the penumbral imaging technique first used in ICF to image the x-ray emission.[114] The measurement principle is illustrated in Fig. 19. Protons are imaged onto a stack of CR-39 detectors a distance ML away from the imaging aperture, using a penumbral aperture larger than the expected emission source size placed at a distance L from the experiment; M is the resulting magnification. A computer aided design (CAD) model of the hardware typically used for fielding is shown in Fig. 20. The emission profile information is encoded in the penumbra of the image and has to be reconstructed through deconvolution. The technique has subsequently also been implemented for use at the NIF,[115] and its utility for 3D imaging of an implosion (using multiple imagers in different LOS) has been demonstrated.[46] It is also advantageous to include IPs in the detector stack behind the CR-39 detectors for simultaneous x-ray imaging.[116] Pinhole imaging is achieved with a similar setup using smaller apertures.[117] The ion beam focus spot in the SNL ion beam ICF program was imaged using an array of pinholes and a differentially filtered CR-39 detector.[5,66]

While traditionally most commonly used for D^{3}He protons, the penumbral imaging technique can, in principle, be adapted to look at any low-Z ion species. In particular, a recent development involves adaptation of the technique for knock-on deuteron imaging (KODI) of DT ICF implosions at OMEGA.[118,119] This has the advantage that the detector filtering can be adapted to look at deuterons of different energy, with the highest-energy KO-d [representing forward scattering, see Eq. (12)] producing an image of the emission source, and lower energy KO-d images of the converged DT shell. Because of high KO-d yields, this implementation has required increasing L and ML to avoid CR-39 saturation.[118] New aperture designs with multiple holes in the same substrate have also been introduced. Multiple-LOS KODI is planned for full 3D tomography of the DT implosion source profile and compressed fuel shape.

As discussed above, ions will lose energy as they traverse the plasma on their way to the detector, complicating analysis compared with neutron imaging. They will also be impacted by electric or
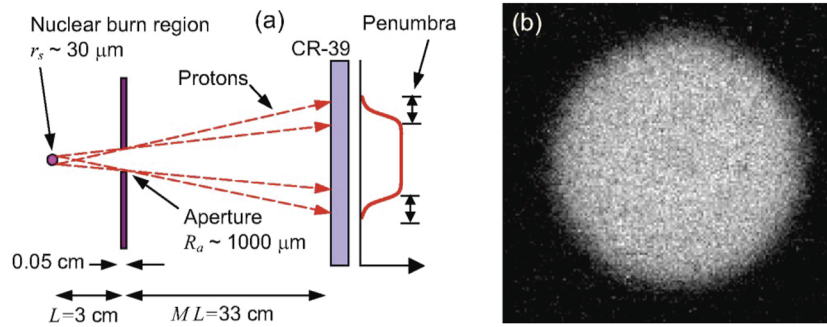
FIG. 19. (a) Schematic of the penumbral ion imaging setup. Source ions are emitted in the nuclear burn region; a penumbral aperture larger than the expected source size at a distance L from the implosion is used to image them onto CR-39 detectors a distance ML from the aperture. Values for L, ML, aperture, and source sizes given in the figure represent typical numbers used at OMEGA, but the numbers as well as the aperture design can easily be varied to adapt to experimental conditions. (b) Example CR-39 image obtained in an OMEGA experiment. The emission profile information is encoded in the image penumbra and has to be reconstructed through deconvolution. Reproduced from Séguin *et al.*, Rev. Sci. Instrum. **75**, 3520 (2004) with the permission of AIP Publishing.
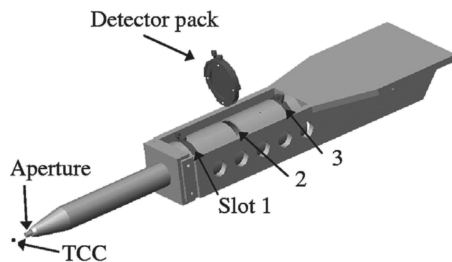

FIG. 20. CAD model of hardware used for penumbral ion imaging at OMEGA. The aperture-TCC distance can be arbitrarily adjusted; the aperture design is adapted to each specific experiment; and the aperture-detector distance can be varied between pre-set options (including slots 1, 2, 3 as well as a further-removed option 349.6 cm out). Reproduced from Kunimune *et al.*, Phys. Plasmas **29**, 072711 (2022) with the permission of AIP Publishing.

magnetic fields around an implosion, including any in the aperture itself; accumulation of negative charge in the aperture, commonly referred to as aperture charging, has been found to distort images, in particular, for lower energy ions, and strategies for mitigation are under development.[119]

VIII. TIME-RESOLVED MEASUREMENTS

The timing and history of nuclear burn relative to the onset of the laser is a key parameter for understanding the dynamics of ICF implosions. Similarly, for basic science experiments, the timing of nuclear emission is often critical. Such information can be obtained through measuring the DT-γ emission history; gas Cherenkov detectors (GCD) and gamma reaction history (GRH) detectors for making this measurement have been implemented at both OMEGA and the NIF.[120] However, these detectors typically require high DT yield. Neutrons or charged particles can instead be used but require a detector fielded close to the implosion for accurate burn history measurements due to finite flight time and relatively broad emission energy spectra (with the time-resolving detector fielded far

from the implosion, the detector instead becomes useful as a spectrometer, such as used in the nTOF concept[9]). A scintillator-based detector for charged-particle burn history measurements has been implemented on OMEGA,[35,121] and a chemical vapor-deposition (CVD) diamond-based detector for charge-particle bang-time measurements on the NIF.[122] Both concepts are described in this section.

A. Scintillator-based detectors

A scintillator-based detector fielded close to TCC with the light relayed to an optical streak camera outside of the target chamber wall for detection was first fielded for neutron burn-history measurements on the Nova laser at Livermore in the 1990s.[123] This system was then adapted for OMEGA, where the Neutron Temporal Diagnostic (NTD) implements the concept for measurements of DD and DT neutron emission history.[43,124] The Proton Temporal Diagnostic[35] (PTD) uses the same principle, but with a nose cone adapted for measurements of D^{3}He protons. The protons interact in a BC422 scintillator fielded 9 cm from the implosion in TIM5, with fast rise time (<20 ps) and slow decay time (~1.2 ns), generating light, which is recorded on a streak camera and deconvolved to obtain the burn history (Fig. 21). This allows differential measurements of shock and compression proton bang time, providing strong constraints on simulations of D^{3}He-gas-filled implosions.

More recently, several different nose cone configurations, including split scintillators with differential filtering optimized for the detection of different particle species and different x-ray energy bands, have been developed for PTD (Fig. 22), with the new unique capabilities of simultaneous nuclear and x-ray burn history measurements captured in the acronym Particle X-ray Temporal Diagnostic[125] (PXTD). PXTD measures the relative timing of multiple nuclear and x-ray burn histories with relative timing uncertainties ±10–20 ps, enabling studies of multi-ion dynamics.[125] The nose cone has also been adapted for focused simultaneous measurements of multiple x-ray energy bands, from which time-resolved T_e can be inferred.[126]
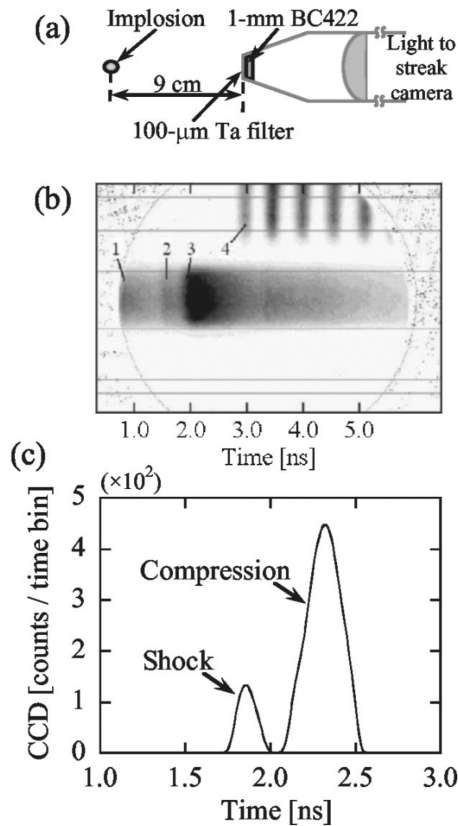
FIG. 21. Early implementation of the Proton Temporal Diagnostic (PTD) at OMEGA. (a) Protons interact in a scintillator close to the implosion, generating light that is relayed to an optical streak camera outside the target chamber wall. (b) x-rays [1], shock [2] and compression [3] protons appear in the resulting streak image, along with a fiducial comb for absolute timing [4]. (c) The image is deconvolved to obtain the proton emission history. Reproduced from Frenje *et al.*, Phys. Plasmas **5**, 2798 (2004) with the permission of AIP Publishing.

B. CVD-diamond-based detectors

At the NIF, the particle time-of-flight[122] (pTOF) detector is used for charged-particle bang time measurements. This detector is a direct analog to the nTOF concept,[9] connecting a fast detector sensitive to impulses of x-rays, neutrons,[127] and ions to oscilloscopes fielded in current mode. pTOF consists of a CVD diamond fielded in a brass housing, with a bias of 500 V applied across it (Fig. 23), and is fielded on the side of a NIF DIM at about 50 cm from TCC (Fig. 13). The detector rise time is of order hundreds of picoseconds. Data are analyzed using an impulse response measured *in situ* on x-ray producing shots. Bang times are inferred with typically ±70 ps accuracy. Because of the relatively long rise time relative to the expected burn duration of most implosions, a burn history is rarely obtained; however, efforts are under way to reduce the rise time in future configurations. pTOF is uniquely capable of measuring nuclear bang time from low yield ($<10^{14}$) implosions at the NIF. This importantly includes surrogate implosions that do not use tritium in the fuel, e.g., pure D_2-gas-filled or D^3He-gas-filled implosions, as well as experiments using a mono-energetic ion backlighter. Accurate knowledge of bang time is often critical to the understanding of these experiments.

Simultaneous measurements of differential shock and compression bang times and areal density (using proton spectrometers) provide a powerful constraint on the dynamics of compression for comparison to radiation-hydrodynamic simulations.[32,129] In principle, pTOF is capable of making the differential shock and compression bang time measurement on D^3He-gas-filled implosions by measuring protons from the shock and DD-n from compression (D^3He protons are often stopped in the imploding target at compression due to high ρR). However, early on, this was found to be challenging due to large x-ray signals obscuring the weak D^3He-p signal. To enable the measurement of a weak proton signal in the presence of x-rays, the capability of fielding a magnet in front of pTOF[129] (the MagPTOF configuration) was implemented, to allow the addition of an x-ray block in the direct LOS from the CVD to TCC with the protons being redirected around the block (Fig. 24).

IX. CHARGED-PARTICLE RADIOGRAPHY

Charged-particle radiography has emerged as a powerful platform for probing subject plasmas generated at laser facilities.[109–111,130–136] Probe ions, typically protons from shock-driven implosions[137] (mono-energetic ion backlighter) or from TNSA,[62] travel through a subject plasma to be detected using an imaging detector or spectrometer. The positively charged probe ions (charge q, velocity v) are sensitive to electric (E) and magnetic (B) fields as well as density fluctuations in the subject plasma, where they
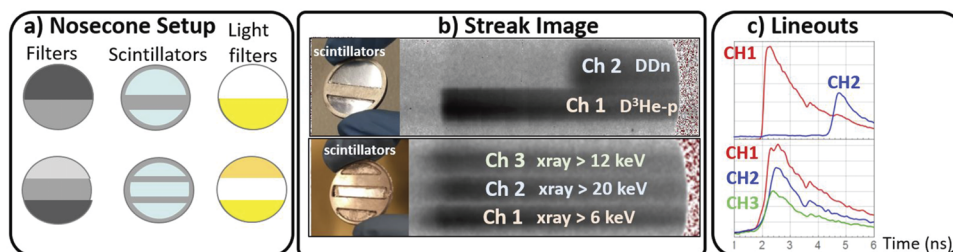

FIG. 22. The modern Particle X-ray Temporal Diagnostic (PXTD) is based on the same principle as PTD (Fig. 21) but uses a split scintillator (a) with differential filtering for optimal detection of different particle species and x-ray energy bands on the same streak camera (b). Panel (c) shows line-outs of the streak images shown in (b). Reproduced from Sio *et al.*, Rev. Sci. Instrum. **87**, 11D701 (2016), with the permission of AIP Publishing.
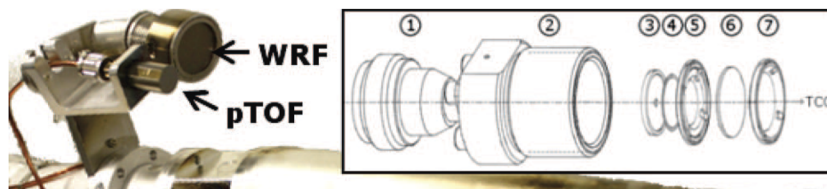
FIG. 23. Schematic of the particle Time-of-Flight (pTOF) detector available at the NIF. The detector consists of a CVD diamond fielded in a brass housing biased to 500 V and coupled to oscilloscopes for current-mode recording of the signal. Reproduced from Rinderknecht *et al.*, Rev. Sci. Instrum. **83**, 10D902 (2012) with the permission of AIP Publishing.
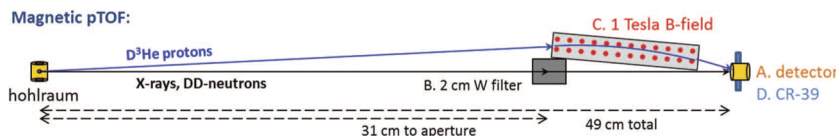

FIG. 24. The pTOF detector can optionally be fielded behind a permanent bending magnet in the MagPTOF configuration, to reduce the fluence of x-rays onto the detector to allow recording of the relatively weaker signal from shock-proton emission. Reproduced from Rinderknecht *et al.*, Rev. Sci. Instrum. **85**, 11D901 (2014) with the permission of AIP Publishing.

will be deflected according the Lorentz force F,

$$F = q[E + v \times B]. \tag{16}$$

While all-encompassing coverage of this rich topic is outside the scope of this paper, no review of ICF and HEDP charged particle diagnostics would be complete without a brief description of this important capability.

A. TNSA backlighter

The TNSA backlighter (Fig. 25) uses a short-pulse laser beam generated using chirped pulse laser amplification[138] (CPA) incident on a foil to produce a directional beam of fast ions, most commonly protons.[62,110] The resulting ions typically follow a near-exponential energy spectrum up to tens of MeV energy,[139] and they are detected using a stack of RCF detectors, with the lower energy ions fully stopped in the initial layers and only the most energetic ones penetrating to the deeper layers. While any ion that penetrates a layer will contribute signal in the RCF, the signal will be dominated by ions at the end of their range, since ions deposit the most energy per unit distance at the Bragg peak. The beam duration is very short, of order
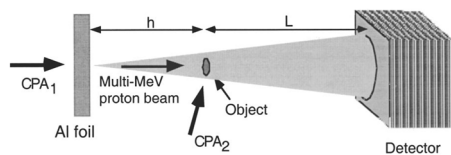

FIG. 25. Schematic of setup for TNSA proton radiography. A CPA-generated short pulse laser beam incident on a metal foil is used to accelerate a beam of protons up to multi-MeV energies in an exponential energy spectrum. The beam penetrates through a subject plasma ("Object") and reaches a stack of RCF detectors recording protons in different energy bands. Reproduced from Borghesi *et al.*, Rev. Sci. Instrum. **74**, 1688 (2003) with the permission of AIP Publishing.

ps, leading to high temporal resolution; ions of different energy traverse the subject plasma at different times, which can be used to diagnose dynamics. Spatial resolution depends on beam divergence, which increases with increasing ion energy.

The OMEGA EP laser can be used to drive a TNSA ion beam either in the OMEGA EP target chamber, with the subject plasma driven by remaining EP beams, or redirected into the OMEGA target chamber, with all 60 OMEGA laser beams available for driving the subject plasma experiment. TNSA at OMEGA/OMEGA EP is a frequently used tool, including for shock propagation studies,[140] probing spherical implosions,[141] studying instability development[135] and magnetic fields and their evolution,[136] and nuclear physics experiments.[109,111] TNSA proton backlighting is also commonly used at other short-pulse laser facilities, e.g., at VULCAN in the UK,[142] but a detailed description of its use at these facilities falls outside the scope of this review.

B. Mono-energetic ion backlighter

The mono-energetic ion backlighter (Fig. 26) uses a number of the laser beams available at a facility such as NIF or OMEGA to implode a thin glass-shell implosion traditionally filled with D^3He gas to generate near-mono-energetic fusion products for use as backlighter probe particles. The concept was originally developed for OMEGA,[137] but has subsequently been implemented on the NIF,[115,143] and has been used for a wide range of subject plasma experiments ranging from imaging of ICF implosions[131] through stopping power studies[133] to laboratory astrophysics applications.[132,134,144] In each case, the subject plasma is driven by a selection of the remaining available laser beams at the facility. Probe ions from the implosion source are emitted into 4π, which means more than one subject plasma can be probed in the same experiment.[130] Sufficient yield for probing depends on the configuration, but typically of order 10^8 is required. This is reliably
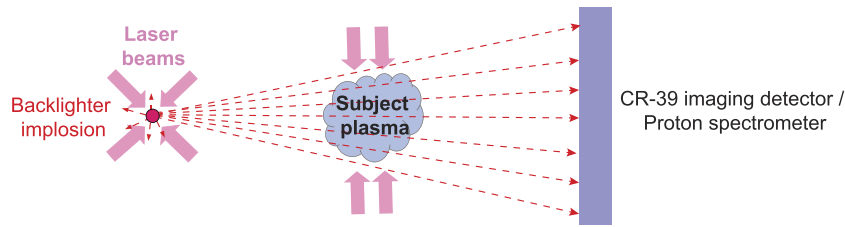
FIG. 26. Cartoon of the mono-energetic charged-particle-backlighter configuration. Near mono-energetic ions (e.g., protons from DD and D^3He fusion reactions) are generated by imploding a gas-filled spherical glass shell using a number of laser beams. Other available laser beams are used to drive a subject plasma. Ions from the backlighter travel through the subject plasma, and are detected either using a CR-39 imaging package (imaging configuration) or a proton spectrometer (stopping power configuration).

obtained with as little as 12 kJ energy (24 of the 60 available OMEGA laser beams) on capsule.[145]

The recording detector can be a spectrometer (e.g., WRF in the case of stopping power experiments[133]), but is most commonly a stack of large (10×10 cm^2) CR-39 imaging detectors with flat metallic filters used to reduce the energy of the source ions to the optimal energy for detection on the CR-39. For many subject plasmas, both the DD-p and D^3He-p from the backlighter penetrate and can be recorded on the CR-39, which helps in breaking the degeneracy between deflections due to E and B. However, with the additional complication of density fluctuations, a third probe particle is extremely helpful for addressing questions about degeneracy. A recent development adds tritium in the backlighter implosion gas fill, hence producing a third mono-energetic charged particle, the T^3He-d [Eq. (5)], in the "tri-particle" backlighter configuration (Fig. 27).[146]

Spatial resolution of order 40 μm and temporal resolution of order 100 ps is typically achieved with the mono-energetic ion backlighter; here, the spatial resolution depends on backlighter source size as measured using PCIS, and the temporal resolution is determined by backlighter burn duration as measured using PTD. PTD at OMEGA or pTOF at the NIF is used for measuring the timing of the backlighter implosion relative to the laser beams, which is required to accurately determine probe time for the subject plasma. Due to their different velocities, the effective subject plasma probe times for the three probe ions will also be different.[146,147]

Mono-energetic ion backlighting has provided unparalleled results on, e.g., fields around ICF implosions[131] and within hohlraums,[148] Rayleigh–Taylor induced fields,[149] magnetic reconnection,[150] scaled astrophysical jets,[144,151] collisionless shocks,[132,152,153] turbulent dynamo,[134] and stopping power.[133]

X. CONCLUDING REMARKS

The existing charged-particle diagnostic suites at the OMEGA and NIF laser facilities, reviewed in this paper, provide a broad range of capabilities for diagnosing ICF and HEDP plasmas, and have been widely employed for experiments ranging from programmatic ICF through nuclear reaction studies to astrophysical jets and magnetic reconnection. OMEGA has robust charged particle diagnostic coverage through the combined availability of spectrometers, including the compact WRF and versatile CPS, Thomson parabola (TPIE), penumbral imaging, the PXTD burn history diagnostic, and radiography platforms. Recent key developments at OMEGA include the addition of PXTD, and the emerging knock-on deuteron imaging capability for 3D tomography of the source and shell in cryogenically layered DT experiments. Coverage at the NIF, while also good, would benefit from capabilities equivalent to the versatile OMEGA
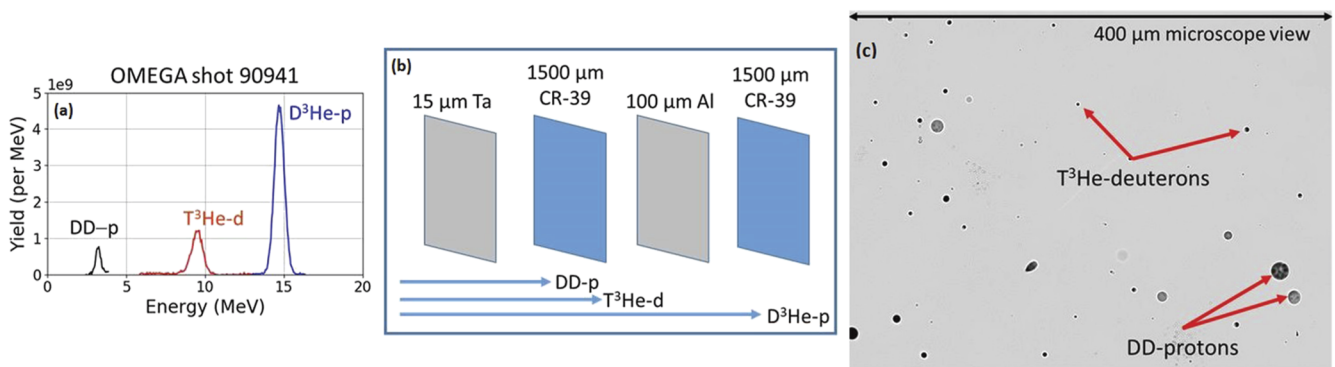

FIG. 27. (a) The "tri-particle" backlighter implosion configuration uses a $D/T/^3He$ gas-fill to generate three quasi-mono-energetic ion species: DD-p, T^3He-d, and D^3He-p. (b) The detector stack is optimized for simultaneous recording of all three particle types. (c) T^3He-d and DD-p are separated on the CR-39 imaging detector based on their track size. Reproduced from Sutcliffe *et al.*, Rev. Sci. Instrum. **92**, 063524 (2021) with the permission of AIP Publishing.

CPS, TPIE, and PXTD diagnostics. The tri-particle mono-energetic ion backlighter development will allow unique results to be obtained at both facilities. As new experiment ideas arise, new technology will be required to enable them; the list already includes a need to measure a low fluence of alpha particles in a background of ablators and protons, which challenges existing technology.

ACKNOWLEDGMENTS

AUTHOR DECLARATIONS

Conflict of Interest

The authors have no conflicts to disclose.

Author Contributions

M. Gatu Johnson: Conceptualization (lead); Writing – original draft (lead).

DATA AVAILABILITY

Data sharing is not applicable to this article as no new data were created or analyzed in this study.

REFERENCES

[1] T. R. Boehly et al., Opt. Commun. **133**, 495 (1997).

[2] J. H. Kelly et al., J. Phys. IV **133**, 75 (2006).

[3] B. M. Van Wontergem et al., Fusion Sci. Technol. **69**, 452–469 (2016).

[4] See www.lasernetus.org for a listing of the facilities within the LaserNetUS and a description of their capabilities.

[5] R. J. Leeper et al., Rev. Sci. Instrum. **59**, 1860 (1988).

[6] F. H. Séguin et al., Rev. Sci. Instrum. **74**, 975 (2003).

[7] J. A. Frenje, Plasma Phys. Controlled Fusion **62**, 023001 (2020).

[8] K. D. Hahn et al., Rev. Sci. Instrum. **85**, 043507 (2014); K. Hahn, "Fusion neutron activation measurements for fast neutron sources in the US," Rev. Sci. Instrum. (submitted).

[9] A. S. Moore et al., "Neutron time of flight (nToF) detectors for inertial fusion experiments," Rev. Sci. Instrum. (submitted).

[10] N. Birge et al., "Neutron imaging of inertial confinement fusion implosions," Rev. Sci. Instrum. **94**, 021101 (2023).

[11] M. Gatu Johnson et al., Phys. Plasmas **24**, 041407 (2017).

[12] A. B. Zylstra et al., Phys. Rev. Lett. **119**, 222701 (2017).

[13] H.-S. Bosch and G. M. Hale, Nucl. Fusion **32**, 611 (1992); **33**, 1919 (1993).

[14] F. H. Séguin et al., Phys. Plasmas **9**, 2725 (2002).

[15] S. J. Gitomer, R. D. Jones, F. Begay, A. W. Ehler, J. F. Kephart, and R. Kristal, Phys. Fluids **29**, 2679 (1986).

[16] S. C. Wilks, A. B. Langdon, T. E. Cowan, M. Roth, M. Singh, S. Hatchett, M. H. Key, D. Pennington, A. MacKinnon, and R. A. Snavely, Phys. Plasmas **8**, 542 (2001).

[17] A. Macchi, M. Borghesi, and M. Passoni, Rev. Mod. Phys. **85**, 751 (2013).

[18] D. G. Hicks et al., Phys. Plasmas **8**, 606 (2001).

[19] N. Sinenian et al., Appl. Phys. Lett. **101**, 114102 (2012).

[20] C. K. Li et al., Phys. Plasmas **8**, 4902 (2001).

[21] J. A. Frenje et al., Phys. Plasmas **9**, 4719 (2002).

[22] H. G. Rinderknecht et al., Phys. Plasmas **22**, 082709 (2015).

[23] M. D. Cable and S. P. Hatchett, J. Appl. Phys. **62**, 2233 (1987).

[24] D. B. Sayre et al., Phys. Rev. Lett. **123**, 165001 (2019).

[25] D. G. Hicks et al., "Charged-particle acceleration and energy loss in laser-produced plasmas," Phys. Plasmas **7**, 5106 (2000).

[26] F. H. Séguin et al., "Measurements of ρR asymmetries at burn time in inertial-confinement-fusion capsules," Phys. Plasmas **9**, 3558 (2002).

[27] N. Sinenian, M. J.-E. Manuel, J. A. Frenje, F. H. Séguin, C. K. Li, and R. D. Petrasso, Plasma Phys. Controlled Fusion **55**, 045001 (2013).

[28] C. J. Waugh, M. J. Rosenberg, A. B. Zylstra, J. A. Frenje, F. H. Séguin, R. D. Petrasso, V. Y. Glebov, T. C. Sangster, and C. Stoeckl, Rev. Sci. Instrum. **86**, 053506 (2015).

[29] C. K. Li et al., Phys. Plasmas **10**, 1919 (2003).

[30] C. K. Li et al., Phys. Rev. Lett. **92**, 205001 (2004).

[31] J. A. Frenje et al., Phys. Plasmas **16**, 042704 (2009).

[32] A. B. Zylstra et al., Phys. Plasmas **21**, 112701 (2014).

[33] A. B. Zylstra et al., Phys.Plasmas **22**, 056301 (2015).

[34] R. D. Petrasso et al., Phys. Rev. Lett. **90**, 095002 (2003).

[35] J. A. Frenje et al., Phys. Plasmas **11**, 2798 (2004).

[36] J. A. Frenje et al., Phys. Rev. Lett. **115**, 205001 (2015).

[37] J. A. Frenje et al., Phys. Rev. Lett. **122**, 015002 (2019).

[38] M. Rosenberg et al., Phys. Plasmas **21**, 122712 (2014).

[39] B. Appelbe and J. Chittenden, Plasma Phys. Controlled Fusion **53**, 045002 (2011).

[40] M. Gatu Johnson et al., Phys. Plasmas **20**, 042707 (2013).

[41] T. J. Murphy, Phys. Plasmas **21**, 072701 (2014).

[42] M. Gatu Johnson et al., Phys. Rev. E **94**, 021202(R) (2016).

[43] C. Stoeckl et al., Rev. Sci. Instrum. **87**, 053501 (2016).

[44] S. F. Khan et al., Proc. SPIE **8505**, 850505 (2012).

[45] F. H. Séguin et al., Rev. Sci. Instrum. **75**, 3520 (2004).

[46] F. H. Séguin et al., Phys. Plasmas **23**, 032705 (2016).

[47] C. Cerjan et al., J. Phys. G: Nucl. Part. Phys. **45**, 033003 (2018).

[48] M. Gatu Johnson et al., Phys. Plasmas **25**, 056303 (2018).

[49] A. B. Zylstra et al., Phys. Rev. Lett. **117**, 035002 (2016).

[50] B. Lahmann et al., Rev. Sci. Instrum. **92**, 083506 (2021).

[51] J. Miyahara, K. Takahashi, Y. Amemiya, N. Kamiya, and Y. Satow, Nucl. Instrum. Methods **246**, 572 (1986).

[52] S. G. Gales and C. D. Bentley, Rev. Sci. Instrum. **75**, 4001 (2004).

[53] N. Izumi, R. Snavely, G. Gregori, J. A. Koch, H.-S. Park, and B. A. Remington, Rev. Sci. Instrum. **77**, 10E325 (2006).

[54] M. J. Rosenberg et al., Rev. Sci. Instrum. **90**, 013506 (2019); Erratum **90**, 029902 (2019).

[55] J. P. Holder et al., Rev. Sci. Instrum. **89**, 10F123 (2018).

[56] H. Chen, A. J. Link, R. van Maren, P. K. Patel, R. Shepherd, S. C. Wilks, and P. Beiersdorfer, Rev. Sci. Instrum. **79**, 10E533 (2008).

[57] J. A. Cobble, K. A. Flippo, D. T. Offermann, F. E. Lopez, J. A. Oertel, D. Mastrosimone, S. A. Letzring, and N. Sinenian, Rev. Sci. Instrum. **82**, 113504 (2011).

[58] C. D. Chen et al., Rev. Sci. Instrum. **79**, 10E305 (2008).

[59] W. L. C. McLaughlin, J. C. Humphreys, D. Hocken, and W. J. Chappas, Nucl. Instrum. Methods Phys. Res. A **302**, 165 (1991).

[60] F. Nürnberg et al., Rev. Sci. Instrum. **80**, 033301 (2009).

[61] M. Borghesi et al., Phys. Plasmas **9**, 2214 (2002).

[62] M. Borghesi, A. Schiavi, D. H. Campbell, M. G. Haines, O. Willi, A. J. MacKinnon, P. Patel, M. Galimberti, and L. A. Gizzi, Rev. Sci. Instrum. **74**, 1688 (2003).

[63] B. G. Cartwright, E. K. Shirk, and P. B. Price, Nucl. Instrum. Methods **153**, 457 (1978).

[64] S. Kacenjar, L. Goldman, and A. Entenberg, Rev. Sci. Instrum. **52**, 831 (1981).

[65] R. J. Leeper, J. R. Lee, L. Kissel, D. J. Johnson, W. A. Stygar, and D. E. Hebron, J. Appl. Phys. **60**, 4059 (1986).

[66] W. A. Stygar et al., Rev. Sci. Instrum. **59**, 1703 (1988).

[67] A. B. Zylstra et al., Rev. Sci. Instrum. **82**, 083301 (2011).

[68] A. B. Zylstra et al., Nucl. Instrum. Methods Phys. Res., Sect. A **681**, 84 (2012).

[69] H. Sio, F. H. Séguin, J. A. Frenje, M. Gatu Johnson, A. B. Zylstra, H. G. Rinderknecht, M. J. Rosenberg, C. K. Li, and R. D. Petrasso, Rev. Sci. Instrum. **85**, 11E119 (2014).

[70] B. Lahmann, M. Gatu Johnson, J. A. Frenje, Y. Y. Glebov, H. G. Rinderknecht, F. H. Séguin, G. Sutcliffe, and R. D. Petrasso, Rev. Sci. Instrum. **91**, 053502 (2020).

[71] N. Sinenian et al., Rev. Sci. Instrum. **82**, 103303 (2011).

[72] F. H. Séguin et al., Rev. Sci. Instrum. **83**, 10D908 (2012).

[73] J. Frenje et al., Rev. Sci. Instrum. **73**, 2597 (2002).

[74] R. Przobocki et al., Rev. Sci. Instrum. **92**, 013504 (2021).

[75] J. Rojas-Herrera et al., Rev. Sci. Instrum. **86**, 033501 (2015).

[76] H. G. Rinderknecht et al., Rev. Sci. Instrum. **86**, 123511 (2015).

[77] M. J.-E. Manuel, M. J. Rosenberg, N. Sinenian, H. Rinderknecht, A. B. Zylstra, F. H. Séguin, J. Frenje, C. K. Li, and R. D. Petrasso, Rev. Sci. Instrum. **82**, 095110 (2011).

[78] M. J. Rosenberg et al., Rev. Sci. Instrum. **85**, 103504 (2014).

[79] G. D. Sutcliffe et al., Rev. Sci. Instrum. **87**, 11D812 (2016).

[80] N. Sinenian et al., Rev. Sci. Instrum. **83**, 043502 (2012).

[81] R. J. Leeper, W. A. Stygar, R. P. Kensek, J. R. Lee, D. J. Johnson, T. R. Lockner, J. Maenchen, D. E. Hebron, and D. F. Wenger, Rev. Sci. Instrum. **59**, 1700 (1988).

[82] W. A. Stygar, L. P. Mix, and R. J. Leeper, Rev. Sci. Instrum. **62**, 1527 (1991).

[83] D. T. Casey et al., Rev. Sci. Instrum. **84**, 043506 (2013).

[84] J. D. Kilkenny et al., "National Diagnostic Working Group (NDWG) for ICF/HED: The whole exceeds the sum of its parts," Rev. Sci. Instrum. (submitted).

[85] H. Chen, P. K. Patel, D. F. Price, B. K. Young, P. T. Springer, R. Berry, R. Booth, C. Bruns, and D. Nelson, Rev. Sci. Instrum. **74**, 1551 (2003).

[86] H. Chen, S. C. Wilks, P. K. Patel, R. Shepherd, P. T. Springer, R. Berry, R. Booth, C. Bruns, and D. Nelson, Rev. Sci. Instrum. **77**, 10E703 (2006).

[87] D. Mariscal, G. J. Williams, H. Chen, S. Ayers, N. Lemos, S. Kerr, and T. Ma, Rev. Sci. Instrum. **89**, 10I145 (2018).

[88] J. von der Linden, J. Ramos-Méndez, B. Faddegon, D. Massin, G. Fiksel, J. P. Holder, L. Willingale, J. Peebles, M. R. Edwards, and H. Chen, Rev. Sci. Instrum. **92**, 033516 (2021).

[89] H. Chen et al., Rev. Sci. Instrum. **79**, 033301 (2008).

[90] D. G. Hicks, "Charged-particle spectroscopy: A new window on inertial confinement fusion," Ph.D. thesis, MIT, 1999.

[91] Y. Kim et al., Phys. Plasmas **28**, 012707 (2021).

[92] O. M. Mannion et al., Rev. Sci. Instrum. **92**, 033529 (2021).

[93] J. A. Frenje et al., Phys. Rev. Lett. **107**, 122502 (2011).

[94] J. A. Frenje et al., Rev. Sci. Instrum. **79**, 10E502 (2008).

[95] J. A. Frenje et al., Phys. Plasmas **17**, 056311 (2010).

[96] M. Gatu Johnson et al., Rev. Sci. Instrum. **83**, 10D308 (2012).

[97] M. Gatu Johnson et al., Rev. Sci. Instrum. **92**, 023503 (2021).

[98] N. Kabadi, "Exploring evolution of multi-ion effects and electron temperature in ICF implosions at Omega and the NIF," Ph.D. thesis, MIT, 2022.

[99] J. Jeet et al., "Development of a platform for studying solar CNO reactions in an ICF plasma," Front. Phys. (2022) (submitted).

[100] J. Pearcy et al., "Development of Compact Magnetic Spectrometer for use at OMEGA and the National Ignition Facility," (unpublished) (2023).

[101] P. J. Adrian et al., "In-situ calibration of charged particle spectrometers on the OMEGA Laser Facility using ^{241}Am and ^{226}Ra sources," Rev. Sci. Instrum. **93**, 113534 (2022).

[102] J. J. Thomson, Philos. Mag. **13**, 561 (1907).

[103] B. M. Hegelich, B. J. Albright, J. Cobble, K. Flippo, S. Letzring, M. Paffett, H. Ruhl, J. Schreiber, R. K. Schulze, and J. C. Fernández, Nature **439**, 441 (2006).

[104] K. Harres et al., Rev. Sci. Instrum. **79**, 093306 (2008).

[105] C. G. Freeman et al., Rev. Sci. Instrum. **82**, 073301 (2011).

[106] D. Jung et al., Rev. Sci. Instrum. **82**, 013306 (2011).

[107] J. T. Morrison, C. Willis, R. R. Freeman, and L. Van Woerkom, Rev. Sci. Instrum. **82**, 033506 (2011).

[108] N. Sinenian, "Fast-ion spectrometry of ICF implosions and laser-foil experiments at the omega and MTW laser facilities," Ph.D. thesis, MIT, 2013.

[109] C. Stoeckl, C. J. Forrest, V. Y. Glebov, S. P. Regan, T. C. Sangster, W. U. Schröder, A. Schwemmlein, and W. Theobald, Nucl. Instrum. Methods Phys. Res., Sect. A **453**, 41 (2019).

[110] J. Park, J. Kim, G. Cochran, D. Mariscal, R. A. Simpson, A. Zylstra, and T. Ma, Phys. Plasmas **29**, 063106 (2022).

[111] A. K. Schwemmlein, C. Stoeckl, C. J. Forrest, W. T. Shmayda, S. P. Regan, and W. U. Schröder, Nucl. Instrum. Methods Phys. Res., Sect. A **522**, 27 (2022).

[112] N. Sinenian, W. Theobald, J. A. Frenje, C. Stoeckl, F. H. Séguin, C. K. Li, R. D. Petrasso, and R. B. Stephens, Phys. Plasmas **19**, 112708 (2012).

[113] J. L. DeCiantis et al., Rev. Sci. Instrum. **77**, 043503 (2006).

[114] K. A. Nugent and B. Luther-Davies, Opt. Commun. **49**, 393 (1984).

[115] J. R. Rygg et al., Rev. Sci. Instrum. **86**, 116104 (2015).

[116] P. J. Adrian et al., "X-ray-imaging spectrometer (XRIS) for studies of residual kinetic energy and low-mode asymmetries in inertial confinement fusion implosions at OMEGA (invited)," Rev. Sci. Instrum. **93**, 113540 (2022).

[117] A. B. Zylstra et al., Rev. Sci. Instrum. **87**, 11E704 (2016).

[118] H. G. Rinderknecht et al., "A knock-on deuteron imager for measurements of fuel and hot-spot asymmetry in direct-drive inertial confinement fusion implosions," Rev. Sci. Instrum. **93**, 093507 (2022).

[119] J. H. Kunimune et al., Phys. Plasmas **29**, 072711 (2022).

[120] Y. Kim and H. Herrmann, "Gamma ray measurements for inertial confinement fusion applications," Rev. Sci. Instrum. (submitted).

[121] H. Sio et al., Rev. Sci. Instrum. **87**, 11D701 (2016).

[122] H. G. Rinderknecht et al., Rev. Sci. Instrum. **83**, 10D902 (2012).

[123] R. A. Lerche, D. W. Phillion, and G. L. Tietbohl, Rev. Sci. Instrum. **66**, 933 (1995).

[124] C. Stoeckl, V. Y. Glebov, S. Roberts, T. C. Sangster, R. A. Lerche, R. L. Griffith, and C. Sorce, Rev. Sci. Instrum. **74**, 1713 (2003).

[125] H. Sio et al., Phys. Rev. Lett. **122**, 035001 (2019).

[126] N. V. Kabadi et al., "The phase-2 particle x-ray temporal diagnostic for simultaneous measurement of multiple x-ray and nuclear emission histories from OMEGA implosions (invited)," Rev. Sci. Instrum. **93**, 103538 (2022).

[127] N. V. Kabadi et al., Rev. Sci. Instrum. **87**, 11D817 (2016).

[128] J. Lindl, O. Landen, J. Edwards, E. Moses, and NIC Team, Phys. Plasmas **21**, 020501 (2014).

[129] H. G. Rinderknecht et al., Rev. Sci. Instrum. **85**, 11D901 (2014).

[130] C. K. Li et al., Phys. Rev. Lett. **97**, 135003 (2006).

[131] J. R. Rygg et al., Science **319**, 1223 (2008).

[132] C. M. Huntington et al., Nat. Phys. **11**, 173 (2015).

[133] A. B. Zylstra et al., Phys. Rev. Lett. **114**, 215002 (2015).

[134] P. Tzeferacos et al., Nat. Commun. **9**, 591 (2018).

[135] L. Gao et al., Phys. Rev. Lett. **110**, 185003 (2013).

[136] L. Gao et al., Phys. Rev. Lett. **114**, 215003 (2015).

[137] C. K. Li et al., Rev. Sci. Instrum. **77**, 10E725 (2006).

[138]D. Strickland and G. Mourou, Opt. Commun. **56**, 219 (1985).

[139]K. Flippo, T. Bartal, F. Beg, S. Chawla, J. Cobble, S. Gaillard, D. Hey, A. MacKinnon, A. MacPhee, P. Nilson, D. Offermann, S. L. Pape, and M. J. Schmitt, J. Phys.: Conf. Ser. **244**, 022033 (2010).

[140]H. Sio, R. Hua, Y. Ping, C. McGuffey, F. Beg, R. Heeter, C. K. Li, R. D. Petrasso, and G. W. Collins, Rev. Sci. Instrum. **88**, 013503 (2017).

[141]A. B. Zylstra et al., Rev. Sci. Instrum. **83**, 013511 (2012).

[142]A. J. MacKinnon et al., Phys. Rev. Lett. **97**, 045001 (2006).

[143]A. B. Zylstra et al., Rev. Sci. Instrum. **91**, 093505 (2020).

[144]C. K. Li et al., Nat. Commun. **7**, 013081 (2016).

[145]T. M. Johnson et al., Rev. Sci. Instrum. **92**, 043551 (2021).

[146]G. Sutcliffe et al., Rev. Sci. Instrum. **92**, 063524 (2021).

[147]G. D. Sutcliffe et al., Phys. Rev. E **105**, L063202 (2022).

[148]C. K. Li et al., Phys. Rev. Lett. **108**, 025001 (2012).

[149]M. J.-E. Manuel et al., Phys. Rev. Lett. **108**, 255006 (2012).

[150]M. J. Rosenberg et al., Nat. Commun. **6**, 6190 (2015).

[151]C. K. Li et al., Phys. Rev. Lett. **111**, 235003 (2013).

[152]D. B. Schaeffer, W. Fox, R. K. Follett, G. Fiksel, C. K. Li, J. Matteucci, A. Bhattacharjee, and K. Germaschewski, Phys. Rev. Lett. **122**, 245001 (2019).

[153]C. K. Li et al., Phys. Rev. Lett. **123**, 055002 (2019).